Electrochemical Generation of Steady-State Linear Concentration Gradients within Microfluidic Channels Perpendicular to the Flow Field

Pierre Perrodin, Catherine Sella, Laurent Thouin

Electrochemical Generation of Steady-State Linear Concentration Gradients within Microfluidic Channels Perpendicular to the Flow Field

Pierre Perrodin, Catherine Sella, Laurent Thouin*

PASTEUR, Département de chimie, Ecole normale supérieure, PSL University, Sorbonne Université, CNRS, 75005, Paris, France

*** Corresponding author:**
laurent.thouin@ens.psl.eu

Abstract

A new design of microelectrode was introduced to generate electrochemically steady-state linear concentration gradients perpendicular to the flow direction throughout the cross section of microchannels. The shape and geometry of the electrode were established based on operating regimes at microchannel electrodes. Before implementation, optimal conditions were preliminary delineated by numerical simulations according to the flow velocity and microchannel dimensions. To assess experimentally these predictions, a specific microfluidic platform was developed with optimized geometry to simultaneously allow the generation of linear concentration gradients and the mapping of concentration profiles by confocal fluorescence microscopy. As a model, the electrochemical reduction of a quinone in presence of fluorescein was selected to both generate and monitor a linear proton gradient. A good agreement was observed between theoretical and experimental data, establishing the proof of concept. These results should broaden the performance and applications of electrochemical platforms, particularly in the field of active control of microenvironments in biology, biochemistry and analytical chemistry.

INTRODUCTION

Concentration gradients play an important role in many biological and chemical processes, such as chemotaxis, drug screening, volumetric titration, surface patterning, and microfabrication. They can be easily produced by microfluidic microchannel networks[1, 2] in particular to investigate physiological and pathological processes ranging from immune response,[3] development,[4] embryogenesis,[5] cancer metastasis[6] to axon guidance.[7] Such experimental platforms are very promising due to a precise control of mass transport and hydrodynamic conditions. They constitute alternative strategies to macroscale methods[8] by achieving unprecedented spatial and temporal resolutions for active control of microenvironments.[9-12] Conventional methods traditionally developed with hydrogels, micropipettes and chambers are non-ideal for establishing chemical and biochemical gradients.[13] They usually produce concentration profiles that are unstable and limited in length scales. Thanks to advanced microfabrication techniques and miniaturization, microfluidic devices allow generating more accurate and reproducible concentration gradients with tailored spatial and temporal profiles down to the single-cell level.[14] In addition, many other operations like species mixing[15, 16] can be coupled ensuring the flexibility and functionality of the platforms while considerably reducing the volumes of analytes.

According to the areas of application, concentration gradients with complex shapes and various patterns are required.[17, 18] They need also to be tuned accurately either under dynamic or steady-state conditions. Several microfluidic platforms have been thus designed to establish concentration gradients in a quantifiable way.[19-21] They are all based on properties of laminar flows in monophasic systems with diffusive mixing of parallel flow streams. Gradient profiles can be produced in 1D[22, 23] and 2D[24, 25] with gradient generators displaying typical Tree-shape structures.[26] In this case, the number of inlets and parallel steams determines the gradient resolution[27] whereas the combination of structures enables the generation of complex profiles. However, although the time-constant of these generators is small, the circuits occupy substantial space on the chip. Structures with Y-shape overcome this issue[28] but the useful region is limited to a short portion of the main channel where only sigmoidal gradients are generated perpendicular to the flow field. To separate the location of gradient generation from flowing streams, other generators apply passive diffusion through two-compartment diffusion chambers,[29-31] a

flow barrier of membranes[32] or hydrogels.[33, 34] Shear stress induced by flow is eliminated with these generators but larger time constants are reached compared to convective ones. Only hybrid systems can produce gradients in a relatively fast way by pressure balance to decouple flow around diffusion chambers.[35, 36] Hence, despite the ease to yield output concentration gradients, the reliability of these generators relies on continuous fluid replenishment with precise control and adjustment of fluid in parallel streams. Moreover, even if the accuracy is improved by increasing the number of splitting steps, this approach requires large networks and leads to greater risks of blocking or leakage due to high driving pressure.

Alternative strategies to the diffusive mixing of parallel flow streams can be developed by generating electrochemically concentration gradients in a single microfluidic channel. Indeed, as soon as species are electroactive, an electrode within a microchannel can be used to locally monitor and control their concentrations. Compared to microfluidic generators described above, the advantage will undoubtedly be the use of a unique microchannel, allowing rapid formation of concentration gradients while preventing issues related to multiple and parallel microchannels. In this context, electrochemical techniques can be exploited in microfluidic platforms not only for passive sensing[37-45] but also for active control of microenvironments.[46-48] The potential of electrochemistry in exerting precise modulations of concentration in constrained volumes has been successfully demonstrated for example to control dynamically the pH[46, 47] or the on-demand oxygen generation.[48] Concentration gradients can be established in laminar flow using a two-electrode configuration.[49-51] In a previous study, we demonstrated that using a microband electrode as working electrode, concentration gradients can be produced dynamically along a microchannel under Taylor-Aris dispersion.[52] Thus, concentration gradients of different shapes and amplitudes can be generated to allow a sequence of various stimulus patterns at a specific location within the microchannel. In other studies, we showed that concentration gradients can be also implemented from steady-state diffusion layers.[53, 54] Under these conditions, shapes of gradients are arbitrary. They result from different operating regimes at electrodes that determine their amplitude in concentration and size. In the present study, the objective will be to design an electrochemical generator in order to produce steady-state concentration gradients perpendicular to the

flow field. This approach is original since it relies on specific electrode geometries (Figure 1) able to modulate downstream the concentrations of generated species throughout the cross section of the microchannel. To this end, a theoretical approach will be developed based on known operating regimes of microchannel electrodes under laminar flow. In particular, these regimes will be considered to design an electrode with optimized geometry in order to produce transverse linear concentration gradients. Numerical simulations will be carried out both to assess the performance of these gradient generators and to delineate their optimal operating conditions. The predictions will be compared to experimental measurements. A specific microfluidic device will be designed to simultaneously generate concentration gradients and map their profiles by confocal fluorescence light microscopy. As a proof of concept, a gradient of proton will be established by electrochemically reducing a quinone in presence of fluorescein.[55, 56] Fluorescein is a common fluorophore that exhibits a pH-sensitive fluorescence signal to monitor proton gradients.

EXPERIMENTAL SECTION

Materials. Aqueous solutions of $8\ 10^{-6}$ mol L^{-1} fluorescein ($C_{20}H_{10}Na_2O_5$, 98.5% Sigma Aldrich) and 10^{-3} mol L^{-1} 1-4 benzoquinone ($C_4H_4O_2$, 98% Sigma Aldrich) was prepared in 0.3 mol L^{-1} potassium chloride (99% Fluka) used as supporting electrolyte. Water was preliminary purified by a Milli-Q purification system. The diffusion coefficient of benzoquinone was equal to $7.8\ 10^{-6}$ cm^2s^{-1}.[57]

Microfluidic devices. The microsystems consisted in PDMS-NOA glass hybrid microdevices specially designed to perform photoelectrochemical measurements in confocal microscopy. As described in Figure 2, it consisted of one microchannel (15 mm length, 800 µm width, 47 µm height) connected at each end to a reservoir (4 mm diameter). The bottom and top of the microchannel were two parallel glass slides, 1 mm thick at the top (Thermoscientific 76 x 26 mm) and 147 µm thick at the bottom (Menzel 30 x 45 mm). The sidewalls were made of NOA 81 (Norland Optical Adhesive 81). For inlet and outlet, two holes were preliminary drilled mechanically into the glass slide (top layer) by projecting silicon carbide beads (20 µm) with a sandblaster (Microjet 1-2-3, Bibol). Two PDMS blocks (several millimeters thick) with engraved reservoirs (about 20 µm height, 4 mm diameter) were bonded irreversibly on the top of each hole by exposing the PDMS blocks and glass slide to air plasma (Harrick)

before assembling. A PDMS stamp was fabricated by casting a 10:1 mixture (polymer-to-curing agent ratio) of polydimethylsiloxane (PDMS, RTV-615; Momentive Performance Materials) onto a patterned mold of SU-8 2010 photoresist (Microchem). The resulting PDMS stamp comprised on its surface the negative design of the microchannel with its two reservoirs. Its thickness was controlled by profilometry. This design was transferred on the previous glass sheet by applying the stamp on its surface. For that purpose, the whole assembly (stamp and glass sheet) was positioned vertically and a drop of NOA was deposited on the top in order to fill by gravity after several hours the cavities produced between the stamp and the glass slide. After complete filling of the cavities and before removing the PDMS stamp, the assembly was exposed to UV (LC5 Hamamatsu, 15 $mWcm^{-2}$) during 15 s for NOA bonding on glass. Three platinum electrodes (Ti/Pt with 20 nm /40 nm thickness) were patterned on the second glass slide by soft lithography and were deposited using a sputtering coater (K675XD; Emitech). The glass slide was assembled face to face with the former slide by positioning the microchannel perpendicular to the electrodes. Finally, the whole assembly was UV insolated during 130 s for complete bonding. Connecting tubes were additionally punched in the PDMS blocks for inlet and outlet (Figure 2B).

The electrodes were incorporated in the microchannel according to the configuration reported in Figure 2A. The reference electrode (RE) and the counter electrode (CE) were 50 µm and 500 µm width respectively. The working electrode with particular geometry was located between RE and CE at a distance of about 1 mm from each electrode. After fabrication, the microstructures were checked optically under optical microscope.

Electrochemical measurements. All electrochemical experiments were performed at room temperature using a homemade multipotentiostat adapted from an original design.[58] The solution of benzoquinone and fluorescein was flowing continuously within the microchannel. The flow was pressure driven by means of a syringe pump (Harvard Apparatus, type 11 Pico Plus). The average flow velocities were calibrated following a known procedure.[59] During the electrochemical generation of concentration gradient, the working electrode WE was biased at E = -0.3 V/RE on the reduction plateau of benzoquinone.

Confocal fluorescence microscopy. Optical measurements were performed using a laser scanning microscope (LSM 710, Zeiss) equipped with an immersion objective (Plan Apochromat 63x/1.4 Oil DIC 27). The working distance was 0.19 mm. A compromise was achieved between resolution and intensity by optimizing the confocal aperture before experiments. The excitation wavelength of fluorescein was λ = 490 nm. Fluorescein was excited using the 488 nm laser line of argon laser of sufficiently low power to avoid photobleaching and local increase of temperature. Emitted fluorescence was measured at 520 nm. Mapping were acquired using ZEN software (Zeiss) at three different vertical distances within the microchannel z = 13.5, 23.5 and 33.5 µm. The vertical position from the bottom of the microchannel was corrected from optical aberrations by taking into account the difference in refractive index between water and glass. At each vertical distances, a surface area (200 µm x 200 µm) was probed in (*x*,*y*) plane leading to the achievement of (512 x 512) data with 0.415 µm resolution in *x* and *y*-axis. Therefore, each profile of fluorescence intensity established as a function of *y* resulted from 512 data, each of them being the average of 512 data in *x*-axis.

Numerical simulations. Concentration profiles and current responses of electrodes were numerically evaluated by solving in 3D space the mass transport equation under laminar regime with appropriate boundary conditions. A 3D parabolic velocity profile was considered in the flow direction. COMSOL Multiphysics 5.4 software was used to perform finite element simulations with the introduction of appropriate dimensionless parameters.

RESULTS AND DISCUSSION

Principle. In order to optimize the electrode geometry for generating transverse linear concentration gradients (Figure 1B), operating conditions in steady-state regime must be first investigated according to the hydrodynamic regime and confinement effect near the electrodes. Hereafter, the flow is assumed to be laminar. The aspect ratio of the microchannel is high enough *(viz*., width l >> height h) to minimize the contribution of sidewalls.[60]

Dimensionless parameters were introduced for:

- coordinates $X = \frac{x}{h}$, $Y = \frac{y}{h}$ and $Z = \frac{z}{h}$,

- microchannel width $L = \frac{l}{h}$,

- electrode size $W(Y) = \frac{w(y)}{h}$,

- concentration $C = \frac{c}{c_0}$, where c_0 is the initial concentration of species at the entrance of the microchannel,

- and flow velocity by the Peclet number $Pe = \frac{u_{av} h}{D}$, where u_{av} is the average velocity and D the diffusion coefficient of species.

The operating regimes at a regular microband electrode (Figure 1A) were first considered to account for the influence of confinement at electrodes. Three main regimes (I, II and III) were identified as a function of the electrode size W and flow velocity Pe.[53] They are reported in a zone diagram in Figure 3A. Regime I, observed at low Pe and large W, corresponds to the thin layer regime where all electroactive species at the entrance of the microchannel are consumed at the electrodes. Conversely, regime III, at relatively high Pe and low W, corresponds to the so-called Levich regime. This latter is a convective regime while the former is a diffusion one. Regime II, which prevails between I and III, is intermediate with a predominance of both diffusion and convection. According to these regimes, a regular microband electrode can generate electroactive species downstream with output concentrations C_h ranging between 0 and 1. C_h are concentrations established after flow homogenization beyond a minimal distance G_h downstream of the electrode. Simulated variations of C_h are given in Figure 3B as a function of the ratio W/Pe. As expected, highest concentrations are reached in regime I while lowest concentrations achieved in regime III. This property is precisely the one that need to be considered in order to modulate downstream the concentration C_h. Thus, to generate a linear concentration gradient perpendicular to the flow field, the electrode width W should vary with the coordinate Y to fulfill the condition:

$$C_h = \frac{Y}{L} \tag{1}$$

This amounts to replacing in Figure 3B the coordinate C_h by the ratio Y/L to establish first the variation of W/Pe throughout the channel cross section. Figure 3C shows this variation imposed by mass transport

within microchannels of high aspect ratios. The electrode width $W(Y)$ along the channel section can be deduced if a value of Pe is introduced. Note in Figure 3C that all the operating regimes from zones I to III are implemented by the electrode. Regime II is predominant as its contribution covers more than 90 % of the channel width L. If the upstream edge of the electrode is straight (see in Figure 1B), Figure 3C already describes its profile or geometry. Hence, the electrode geometry is fixed from dimensionless parameters, which are the flow velocity Pe and microchannel width L.

Theoretical electrode profile. In the following, an analytical equation of $W(Y)$ was derived from simulated data with:

$$W(Y) = \left[Pe\left(\frac{Y}{1.468L} \right)^{3/2} \right] f(Y) \tag{2}$$

Eq 2 has two terms. The first one corresponds to Levich regime (regime III) while the second is a function $f(Y)$ accounting for the transition between Levich and thin layer regimes (regime I). $f(Y)$ was established from a parametric fit of simulated data. Since W/Pe tends to infinity when $Y/L = 1$, the limit $W/Pe = 2$ between regimes II and I was arbitrary chosen as the boundary condition for $f(Y)$ determination. In this case, it led to:

$$f(Y) = 1 + 2.557\exp\left(8.237\left(\frac{Y}{L} - 1 \right) \right) \tag{3}$$

As shown in Figure 3C, the ratio $W(Y)/Pe$ obtained by eqs 2 and 3 fits the simulated data, except for Y/L very close to 1. In this case, $W(Y)/Pe$ does not tend to infinity but to the maximum value $W_{max}/Pe = 2$, where W_{max} is the widest width of electrode.

The electrode geometry is also reported in Figure 4A. In this figure, the blue curve depicts the profile of the downstream edge of electrode derived from eqs 2 and 3 while the grey area stands for the whole electrode surface area. This electrode geometry was considered for simulations of concentration gradients generated downstream by the electrode. One example with $L = 40$ and $Pe = 40$ illustrates in Figure 4B the concept for generating steady-state linear concentration gradients perpendicular to the flow direction. The concentration gradient is fully established at minimal distances from the downstream edge of electrode.

Simulated performance of electrodes. The concentration gradient is established downstream only when local concentrations become homogeneous over the microchannel height. Simulations showed that this condition is reached at a minimum distance G_h from the electrode (Figure 1A) equal to:

$$G_h = \frac{g_h}{h} = 0.4Pe \quad (4)$$

where G_h is defined from the widest edge of the electrode. Figure 5A gives some concentration gradients simulated at distance G_h under various conditions (W_{max}, Pe). As expected, concentration gradients in Figure 5A are all superimposed and linear throughout the cross section of the microchannel. However, small deviations are observed for $Y/L < 0.04$ and $Y/L > 0.96$ due to the influence of axial diffusion close to the sidewalls. Note that axial diffusion locally re-homogenizes the solution over distances Y/L that exceed one channel height. At distance G_h, this effect is already greater than the influence of velocity profile expected near sidewalls.[60] These deviations increase at distances higher than G_h (Figure 5B). However, up to 100 G_h the concentration gradients remain linear in the central portion of the microchannel. Full homogenization of flow at the concentration $C_h = 0.5$ is expected for distances higher than 1600 G_h. Therefore, these results show that linear concentration gradients can be generated transversally from minimal distances G_h. Apart from the sidewall effects due to axial diffusion, the gradients retain downstream their shape and amplitude up to 100 G_h (Figure 5B).

Alteration of gradient linearity can be also evaluated when flow velocity Pe deviates from its optimal value $Pe_{opt} = W_{max}/2$. The Influence of Pe is illustrated in Figure 6A for a given W_{max},. Two distinct behaviors are observed. When $Pe < Pe_{opt}$, concentrations $C(Y)$ are higher than those predicted at Pe_{opt}. Conversely, when $Pe > Pe_{opt}$, concentrations $C(Y)$ are lower but deviate less in comparison. In order to quantify these deviations, linear correlation coefficients R^2 were calculated under various conditions (W_{max}, Pe) and plotted in Figure 6B as a function of Pe and Pe_{opt}. In this 3D plots, the surface (R^2, Pe, Pe_{opt}) confirms that lower deviations from gradient linearity takes place when $Pe \geq Pe_{opt}$. Therefore, this allows access experimentally to a wider range of Pe (other than Pe_{opt}) to generate linear concentration gradients without the need to control drastically the flow velocity.

Experimental conditions for mapping concentration gradients. The electrochemical reduction of 10^{-3} mol L^{-1} benzophenone (BQ) in presence of 8 10^{-6} mol L^{-1} fluorescein was chosen to investigate experimentally concentration gradients of protons by confocal fluorescence microscopy.[55, 56] Reduction of BQ at electrode leads locally to an increase of pH by consumption of protons such as:

$$BQ + 2e^- + 2H^+ \rightleftharpoons HQ \quad (5)$$

In this experimental setup, the medium cannot be easily degassed. Dissolved oxygen participates also to the process with:

$$O_{2\,(aq)} + 4e^- + 4H^+ \rightleftharpoons 2H_2O \quad (6)$$

However, oxygen contribution is weak at the potential selected for BQ reduction (E =-0.3 V/RE) (see Figure 9A). Concentration of dissolved oxygen is also one order of magnitude lower than BQ concentration. Under these conditions, unbuffered solutions of fluorescein exhibit pH-sensitive fluorescence signals that allow probing proton concentrations. At pH > 5, fluorescein (FH) undergoes the following dissociation step:

$$FH \rightleftharpoons F^- + H^+ \qquad pKa = 6.0 \quad (7)$$

The deprotonated form F^- absorbs at $\lambda = 490$ nm and fluoresces at $\lambda = 520$ nm with much higher intensity than FH.[61] At pH > 7, a relationship between F^- and H^+ concentrations is derived from eq 7 with:

$$[F^-] = C^0_{HF} - 7.3\ 10^{-6}\ [H^+] \qquad R^2 = 0.99938 \quad (8)$$

This function is affine and ensures direct monitoring of concentration gradients during BQ reduction. The BQ-HF mixture was set initially at pH = 7 in order to investigate experimentally any increase in pH by the generation of concentration gradient.

The influence of mismatches in refractive index between glass and water was also considered prior to the mapping of concentration gradient. For that purpose, fluorescence intensity was monitored by confocal microscopy inside the microdevice preliminary filled by a solution of BQ-HF mixture. Measurements were performed along the microchannel height without polarizing the electrode. A profile

of fluorescence intensity was established as a function of the vertical distance z given by the translation of the objective relative to the microdevice position. The profile given in Figure 7A clearly demonstrates the issue of focused incident beam thanks to the difference in refractive index. On the one hand, the effective vertical position z' of the focus point at which the solution is probed inside the microchannel is shifted to lower values respective to the position z. Indeed, at small beam angles, the first refraction law affords:

$$\frac{z}{z'} \approx \frac{n_{\text{glass}}}{n_{\text{water}}} = \frac{1.52}{1.33} \tag{9}$$

After a complete scan of the microdevice section, it led in Figure 7A to an overestimation of the microchannel height h. On the other hand, the fluorescence intensity decreases as a function of z, demonstrating a variation with z of the sampled volume delineated by confocal microscopy. To assess quantitatively the influence of refractive index on such measurements, a drop of fluorescein solution was deposited on a glass slide similar to the one of the microdevice. Fluorescence intensity was also monitored as a function of z (Figure 7B). As in Figure 7A, the same trend was observed but over a wider range of z, enabling a calibration curve to be established for vertical distances z of interest. This calibration curve in association with eq 9 allow thus accounting for the mismatch in refractive index and evaluating their effects on optical measurements. To check the calibration, data in Figure 7A were processed accordingly. Fluorescence intensity was corrected by dividing each value by the one issued from the calibration curve at the corresponding distance z. These corrected values, $i_{\text{F cor}}$ were then plotted in Figure 7C as a function of z' using eq 9. Within the experimental uncertainties, $i_{\text{F cor}}$ was almost constant within the microchannel as expected for a homogenous solution of BQ-HF mixture. Furthermore, the width of $i_{\text{F cor}}$ plateau corresponded to the nominal microchannel height h. These observations confirmed experimentally the above assumptions and procedure defined for reconstructing the concentration profile from fluorescence intensity measurements.

Figure 8 shows a schematic representation of the experimental setup. The electrode was designed according to the theoretical profile established by eqs 2 and 3 with $Pe = 40$ and $L = 40$. Assuming that the microchannel height was $h = 50$ µm, this corresponded to an electrode size

w_{max} = 4000 µm and to a microchannel width l = 2000 µm. However, for practical reasons, theses dimensions could not be envisaged experimentally. Large platinum electrodes as well as large microchannels often lead experimentally to fluid leakages inside the microdevices. To overcome these issues, we only considered a part of the electrode profile within a narrower microchannel. Therefore, by setting l = 800 µm, the electrode profile was theoretically exposed from $w(y) = 0$ to w^*_{max} = 300 µm. An optical image showing the experimental setup is provided in Figure 8B. After microfabrication the characteristics of the microdevice were slightly different due to the inherent microfabrication procedures. The microchannel position with respect to the electrode profile was misaligned with a slight tilt. After microfabrication, the width and height of the microchannel were 780 µm and 47 µm respectively, values that were close to the nominal values (*viz*., 800 µm and 50 µm). Assuming for HQ a diffusion coefficient $D = 7.8\ 10^{-6}$ cm^2s^{-1},[57] the optimal flow rate corresponding to Pe = 40 was 1.5 µL min^{-1}. The misalignment between the microchannel and the profile of electrode was not so critical since the position of the area probed by confocal microscopy was defined with respect to the electrode profile and not relative to the position of the microchannel sidewalls (*see* Figure 8B). The probed area was located at an average distance exceeding 880 µm, which was higher than the distance g_h = 752 µm evaluated under these conditions (eq 4). The size and location of the probed area were defined in order to monitor significant variations of fluorescence light intensity over limited time durations. This area was positioned away from the microchannel sidewalls to discard their influence on mass transport. Hence, the probed area was a square of 200 x 200 µm as schematized in Figure 8B (dashed area). Measurements were monitored and data were averaged from numerous scans as described in experimental section. It must be emphasized that the accuracy of these electrochemical tests was conditioned by the stability of the electrode performance. As long as no significant electrode passivation took place and that flow was well controlled, concentration gradients could be produced for several minutes to allow the mapping by confocal microscopy. Concentration gradients could be reproduced several times to perform measurements at different vertical distances within the microchannel.

Experimental performance of the microdevice. Steady state concentration gradients were established by probing the fluorescence light intensity at three vertical distances z. For each z, mean data

were calculated from 512 scans along *x*-axis and they were plotted as a function of *y* (Figure 9A). As observed, profiles resulting from fluorescence measurements were almost linear irrespective of the vertical distance *z*. Within experimental uncertainties, linear regressions were obtained with *R* values higher than 0.975. As demonstrated above, fluorescence intensities depend on *z* due to the influence of refractive indexes on focused beam. By considering the calibration curve in Figure 7B, data were thus corrected to fit the intermediate position $z = 26.9$ µm ($z' = 23.5$ µm). As shown in Figure 9B, corrected profiles were superimposed. Linear variations were observed over 200 µm distance, eliminating any influence of refractive index. In comparison, the theoretical concentration gradient corresponding to these experimental conditions was also plotted with concentrations *C* of generated hydroquinone HQ ranging between 0.25 and 0.4. A fit of data was performed to match the scales between fluorescence light intensity and concentration. Note that the relationship obtained between fluorescence light intensity and concentration depends on many experimental parameters including the fine-tuning of the confocal microscope before each series of measurements. Finally, in order to support all these results, the electrode current was investigated experimentally according to the flow velocity. In this case, the electrode current can be also simulated and predicted accurately. In Figure 9C, electrode currents were monitored for flow rates encompassing the optimal value of 1.5 µl min^{-1} for the microdevice. Experimental currents were then compared to currents simulated for the two-electron reduction of benzoquinone BQ (eq 5). A very good agreement was observed between data, thus validating again the predictions and the underlying conditions for generating linear concentrations gradients. These results with those reported in Figure 9B support the concept introduced in the present work. Note that this concept is not limited only to the generation of linear gradients since more complex concentration gradients can be envisaged using a similar approach. Whatever the gradient profile, steady-state and transverse concentration gradients can be easily electrogenerated.

CONCLUSION

Electrodes were designed for generating in microchannels steady-state linear concentration gradients, perpendicular to the flow direction. Based on operating regimes identified at microchannel electrodes, the electrode geometry was optimized theoretically by considering an infinity of

experimental conditions. According to the microchannel characteristics, numerical simulations demonstrated that the performance of these electrodes was optimal for a given range of flow velocity, making easier their implementation in microfluidic platforms. This approach was investigated experimentally by generating linear proton gradients through the electrochemical reduction of a quinone. The concentration gradients were successfully monitored by confocal fluorescence microscopy, showing a good linearity in concentration profiles over a selected area of the microchannel. These results were also supported by monitoring the electrode current as a function of flow velocity. In this case, the good agreement observed between theoretical and experimental data clearly established the proof of concept and the underlying conditions for producing concentration gradients of any profile. In comparison to microfluidic generators, concentration gradients are generated without any splitting steps and parallel streams up to the gradient location. The implementation of steady state gradients is relatively fast due to the short diffusion lengths required. Furthermore, it does not require an accurate control of flow velocity and pressure balance within the microfluidic circuit. As soon as concentration gradient can be generated, directly or indirectly from electroactive species, this concept is valid and opens undoubtedly new perspectives in microfluidics for investigating the influence of active microenvironments on biological processes or modulation of concentration for analytical purposes.

ACKNOWLEDGMENTS

This work was supported in parts by CNRS UMR 8640, ENS (Ecole normale superieure), PSL University and Sorbonne Université. P.P thanks the doctoral school ED388 for a Ph. D. grant. Geraldine Hallais is acknowledged for her support in the design and fabrication of the microdevices.

REFERENCES

1. Toh, A. G. G.; Wang, Z. P.; Yang, C.; Nguyen, N.-T., Engineering microfluidic concentration gradient generators for biological applications. *Microfluid. Nanofluid.* **2014,** *16* (1-2), 1-18.
2. Wang, S.; Chen, X., Simulation and experimental investigation on tree concentration gradient generator with U-shape microchannel. *Microsyst. Technol.* **2018,** *25* (3), 1111-1119.
3. Foley, J. O.; Nelson, K. E.; Mashadi-Hossein, A.; Finlayson, B. A.; Yager, P., Concentration gradient immunoassay. 2. Computational modeling for analysis and optimization. *Anal. Chem.* **2007,** *79* (10), 3549-53.
4. Gupta, K.; Kim, D. H.; Ellison, D.; Smith, C.; Kundu, A.; Tuan, J.; Suh, K. Y.; Levchenko, A., Lab-on-a-chip devices as an emerging platform for stem cell biology. *Lab. Chip* **2010,** *10* (16), 2019-31.
5. Heo, Y. S.; Cabrera, L. M.; Bormann, C. L.; Shah, C. T.; Takayama, S.; Smith, G. D., Dynamic microfunnel culture enhances mouse embryo development and pregnancy rates. *Hum. Reprod.* **2010,** *25* (3), 613-22.
6. Saadi, W.; Wang, S. J.; Lin, F.; Jeon, N. L., A parallel-gradient microfluidic chamber for quantitative analysis of breast cancer cell chemotaxis. *Biomed. Microdevices* **2006,** *8* (2), 109-18.
7. Xiao, R. R.; Zeng, W. J.; Li, Y. T.; Zou, W.; Wang, L.; Pei, X. F.; Xie, M.; Huang, W. H., Simultaneous generation of gradients with gradually changed slope in a microfluidic device for quantifying axon response. *Anal. Chem.* **2013,** *85* (16), 7842-50.
8. El-Ali, J.; Sorger, P. K.; Jensen, K. F., Cells on chips. *Nature* **2006,** *442* (7101), 403-11.
9. Weibel, D. B.; Whitesides, G. M., Applications of microfluidics in chemical biology. *Curr. Opin. Chem. Biol.* **2006,** *10* (6), 584-91.
10. Mark, D.; Haeberle, D., Microfluidic lab-on-a-chip platforms: requirements, characteristics and applicatons. *Chem. Soc. Rev.* **2010,** *39* (3), 1153-1152.
11. Velve-Casquillas, G.; Le Berre, M.; Piel, M.; Tran, P. T., Microfluidic tools for cell biological research. *Nano Today* **2010,** *5* (1), 28-47.

12. Beta, C.; Bodenschatz, E., Microfluidic tools for quantitative studies of eukaryotic chemotaxis. *Eur. J. Cell. Biol.* **2011,** *90* (10), 811-6.

13. Keenan, T. M.; Folch, A., Biomolecular gradients in cell culture systems. *Lab. Chip* **2008,** *8* (1), 34-57.

14. Awwad, Y.; Geng, T.; Baldwin, A. S.; Lu, C., Observing single cell NF-kappaB dynamics under stimulant concentration gradient. *Anal. Chem.* **2012,** *84* (3), 1224-8.

15. Chen, X.; Li, T.; Zeng, H.; Hu, Z.; Fu, B., Numerical and experimental investigation on micromixers with serpentine microchannels. *Int. J. Heat Mass Transf.* **2016,** *98*, 131-140.

16. Chen, X.; Shen, J., Numerical analysis of mixing behaviors of two types of E-shape micromixers. *Int. J. Heat Mass Transf.* **2017,** *106*, 593-600.

17. Li Jeon, N.; Baskaran, H.; Dertinger, S. K.; Whitesides, G. M.; Van de Water, L.; Toner, M., Neutrophil chemotaxis in linear and complex gradients of interleukin-8 formed in a microfabricated device. *Nat. Biotechnol.* **2002,** *20* (8), 826-30.

18. Ahmed, T.; Shimizu, T. S.; Stocker, R., Bacterial chemotaxis in linear and nonlinear steady microfluidic gradients. *Nano Lett.* **2010,** *10* (9), 3379-85.

19. Kim, S.; Kim, H. J.; Jeon, N. L., Biological applications of microfluidic gradient devices. *Integr. Biol.* **2010,** *2* (11-12), 584-603.

20. Somaweera, H.; Ibraguimov, A.; Pappas, D., A review of chemical gradient systems for cell analysis. *Anal. Chim. Acta* **2016,** *907*, 7-17.

21. Wang, X.; Liu, Z.; Pang, Y., Concentration gradient generation methods based on microfluidic systems. *RSC Adv.* **2017,** *7* (48), 29966-29984.

22. Chen, X.; Hu, Z.; Zhang, L.; Yao, Z.; Chen, X.; Zheng, Y.; Liu, Y.; Wang, Q.; Liu, Y.; Cui, X.; Song, H., Numerical and Experimental Study on a Microfluidic Concentration Gradient Generator for Arbitrary Approximate Linear and Quadratic Concentration Curve Output. *Int. J. Chem. React. Eng.* **2018,** *16* (1).

23. Hu, Z.; Chen, X.; Wang, L., Design and Fabrication of Concentration-Gradient Generators with Two and Three Inlets in Microfluidic Chips. *Chem. Eng. Technol.* **2018,** *41* (3), 489-495.

24. Neils, C.; Tyree, Z.; Finlayson, B.; Folch, A., Combinatorial mixing of microfluidic streams. *Lab. Chip* **2004,** *4* (4), 342-50.

25. Shakeri, A.; Sun, N.; Badv, M.; Didar, T. F., Generating 2-dimensional concentration gradients of biomolecules using a simple microfluidic design. *Biomicrofluidics* **2017,** *11* (4), 044111.

26. Jeon, N. L.; Dertinger, S. K. W.; Chiu, D. T.; Choi, I. S.; Stroock, A. D.; Whitesides, G. M., Generation of Solution and Surface Gradients Using Microfluidic Systems. *Langmuir* **2000,** *16* (22), 8311-8316.

27. Dertinger, S. K. W.; Chiu, D. T.; Jeon, N. L.; Whitesides, G. M., Generation of Gradients Having Complex Shapes Using Microfluidic Networks. *Anal. Chem.* **2001,** *73* (6), 1240-1246.

28. Zhou, Y.; Wang, Y.; Mukherjee, T.; Lin, Q., Generation of complex concentration profiles by partial diffusive mixing in multi-stream laminar flow. *Lab. Chip* **2009,** *9* (10), 1439-48.

29. Saadi, W.; Rhee, S. W.; Lin, F.; Vahidi, B.; Chung, B. G.; Jeon, N. L., Generation of stable concentration gradients in 2D and 3D environments using a microfluidic ladder chamber. *Biomed. Microdevices* **2007,** *9* (5), 627-35.

30. Selimovic, S.; Sim, W. Y.; Kim, S. B.; Jang, Y. H.; Lee, W. G.; Khabiry, M.; Bae, H.; Jambovane, S.; Hong, J. W.; Khademhosseini, A., Generating nonlinear concentration gradients in microfluidic devices for cell studies. *Anal. Chem.* **2011,** *83* (6), 2020-8.

31. Zhou, Y.; Lin, Q., Microfluidic flow-free generation of chemical concentration gradients. *Sens. Actuators ,B* **2014,** *190*, 334-341.

32. Abhyankar, V. V.; Lokuta, M. A.; Huttenlocher, A.; Beebe, D. J., Characterization of a membrane-based gradient generator for use in cell-signaling studies. *Lab. Chip* **2006,** *6* (3), 389-93.

33. Shin, Y.; Han, S.; Jeon, J. S.; Yamamoto, K.; Zervantonakis, I. K.; Sudo, R.; Kamm, R. D.; Chung, S., Microfluidic assay for simultaneous culture of multiple cell types on surfaces or within hydrogels. *Nat. Protoc.* **2012,** *7* (7), 1247-59.

34. Garcia, S.; Sunyer, R.; Olivares, A.; Noailly, J.; Atencia, J.; Trepat, X., Generation of stable orthogonal gradients of chemical concentration and substrate stiffness in a microfluidic device. *Lab. Chip* **2015,** *15* (12), 2606-14.

35. Atencia, J.; Morrow, J.; Locascio, L. E., The microfluidic palette: a diffusive gradient generator with spatio-temporal control. *Lab. Chip* **2009,** *9* (18), 2707-14.

36. Zhou, B.; Xu, W.; Wang, C.; Chau, Y.; Zeng, X.; Zhang, X.-X.; Shen, R.; Wen, W., Generation of tunable and pulsatile concentration gradients via microfluidic network. *Microfluid. Nanofluid.* **2014,** *18* (2), 175-184.

37. Li, Y.; Sella, C.; Lemaître, F.; Guille Collignon, M.; Thouin, L.; Amatore, C., Highly Sensitive Platinum-Black Coated Platinum Electrodes for Electrochemical Detection of Hydrogen Peroxide and Nitrite in Microchannel. *Electroanalysis* **2013,** *25* (4), 895-902.

38. Oliveira, R.; Bento, F.; Sella, C.; Thouin, L.; Amatore, C., Direct electroanalytical method for alternative assessment of global antioxidant capacity using microchannel electrodes. *Anal. Chem.* **2013,** *85* (19), 9057-63.

39. Bellagha-Chenchah, W.; Sella, C.; Fernandez, F. R.; Peroni, E.; Lolli, F.; Amatore, C.; Thouin, L.; Papini, A. M., Interactions between Human Antibodies and Synthetic Conformational Peptide Epitopes: Innovative Approach for Electrochemical Detection of Biomarkers of Multiple Sclerosis at Platinum Electrodes. *Electrochim. Acta* **2015,** *176*, 1239-1247.

40. Horny, M. C.; Lazerges, M.; Siaugue, J. M.; Pallandre, A.; Rose, D.; Bedioui, F.; Deslouis, C.; Haghiri-Gosnet, A. M.; Gamby, J., Electrochemical DNA biosensors based on long-range electron transfer: investigating the efficiency of a fluidic channel microelectrode compared to an ultramicroelectrode in a two-electrode setup. *Lab. Chip* **2016,** *16* (22), 4373-4381.

41. Anderson, M. J.; Crooks, R. M., Microfluidic Surface Titrations of Electroactive Thin Films. *Langmuir* **2017,** *33* (28), 7053-7061.

42. Li, Y.; Sella, C.; Lemaître, F.; Guille-Collignon, M.; Thouin, L.; Amatore, C., Electrochemical Detection of Nitric Oxide and Peroxynitrite Anion in Microchannels at Highly Sensitive Platinum-Black Coated Electrodes. Application to ROS and RNS Mixtures prior to Biological Investigations. *Electrochim. Acta* **2014,** *144*, 111-118.

43. Li, Y.; Sella, C.; Lemaitre, F.; Guille-Collignon, M.; Amatore, C.; Thouin, L., Downstream Simultaneous Electrochemical Detection of Primary Reactive Oxygen and Nitrogen Species

Released by Cell Populations in an Integrated Microfluidic Device. *Anal. Chem.* **2018,** *90* (15), 9386-9394.

44. Wan, H.; Yin, H., Tunable and quantitative serial dilution on multi-channel miniaturized microfluidic electrochemical platform. *Sens. Actuators, B* **2018,** *274*, 682-688.

45. Oliveira, R.; Sella, C.; Souprayen, C.; Ait-Yahiatene, E.; Slim, C.; Griveau, S.; Thouin, L.; Bedioui, F., Development of a flow microsensor for selective detection of nitric oxide in the presence of hydrogen peroxide. *Electrochim. Acta* **2018,** *286*, 365-373.

46. Fomina, N.; Johnson, C. A.; Maruniak, A.; Bahrampour, S.; Lang, C.; Davis, R. W.; Kavusi, S.; Ahmad, H., An electrochemical platform for localized pH control on demand. *Lab. Chip* **2016,** *16* (12), 2236-44.

47. Balakrishnan, D.; Lamblin, G.; Thomann, J. S.; van den Berg, A.; Olthuis, W.; Pascual-Garcia, C., Electrochemical Control of pH in Nanoliter Volumes. *Nano Lett.* **2018,** *18* (5), 2807-2815.

48. Xu, W.; Foster, E.; Ma, C.; Bohn, P. W., On-demand in situ generation of oxygen in a nanofluidic embedded planar microband electrochemical reactor. *Microfluid. Nanofluid.* **2015,** *19* (5), 1181-1189.

49. Cabrera, C. R.; Finlayson, B.; Yager, P., Formation of natural pH gradients in a microfluidic device under flow conditions: model and experimental validation. *Anal. Chem.* **2001,** *73* (3), 658-66.

50. Yoon, S. K.; Fichtl, G. W.; Kenis, P. J. A., Active control of the depletion boundary layers in microfluidic electrochemical reactors. *Lab. Chip* **2006,** *6* (12), 1516-1524.

51. Liu, X.; Abbott, N. L., Lateral transport of solutes in microfluidic channels using electrochemically generated gradients in redox-active surfactants. *Anal. Chem.* **2011,** *83* (8), 3033-41.

52. Abadie, T.; Sella, C.; Perrodin, P.; Thouin, L., Electrochemical Generation and Detection of Transient Concentration Gradients in Microfluidic Channels. Theoretical and Experimental Investigations. *Front. Chem.* **2019,** *7*, 704.

53. Amatore, C.; Da Mota, N.; Sella, C.; Thouin, L., Theory and experiments of transport at channel microband electrodes under laminar flows. 1. Steady-state regimes at a single electrode. *Anal. Chem.* **2007,** *79* (22), 8502-10.

54. Amatore, C.; Lemmer, C.; Sella, C.; Thouin, L., Channel Microband Chronoamperometry: From Transient to Steady-State Regimes. *Anal. Chem.* **2011,** *83* (11), 4170-4177.

55. Cannan, S.; Douglas Macklam, I.; Unwin, P. R., Three-dimensional imaging of proton gradients at microelectrode surfaces using confocal laser scanning microscopy. *Electrochem. Commun.* **2002,** *4* (11), 886-892.

56. Rudd, N. C.; Cannan, S.; Bitziou, E.; Ciani, I.; Whitworth, A. L.; Unwin, P. R., Fluorescence confocal laser scanning microscopy as a probe of pH gradients in electrode reactions and surface activity. *Anal. Chem.* **2005,** *77* (19), 6205-17.

57. Baticle, A. M., Mesure directe des coefficients de diffusion d'ions en solution aqueuse en présence d'un électrolyte support. *J. Electroanal. Chem.* **1964,** *8* (1), 13-19.

58. Maisonhaute, E.; White, P. C.; Compton, R. G., Surface Acoustic Cavitation Understood via Nanosecond Electrochemistry. *J. Phys. Chem. B* **2001,** *105*, 12087-12091.

59. Amatore, C.; Belotti, M.; Chen, Y.; Roy, E.; Sella, C.; Thouin, L., Using electrochemical coupling between parallel microbands for in situ monitoring of flow rates in microfluidic channels. *J. Electroanal. Chem.* **2004,** *573* (2), 333-343.

60. Gorman, B. R.; Wikswo, J. P., Characterization of transport in microfluidic gradient generators. *Microfluid. Nanofluid.* **2008,** *4* (4), 273-285.

61. Sjoback, R.; Nygren, J.; Kubista, M., Absorption and fluorescence properties of fluorescein. *Spectrochim. Acta, Part A* **1995,** *51* (6), L7-L21.

FIGURES

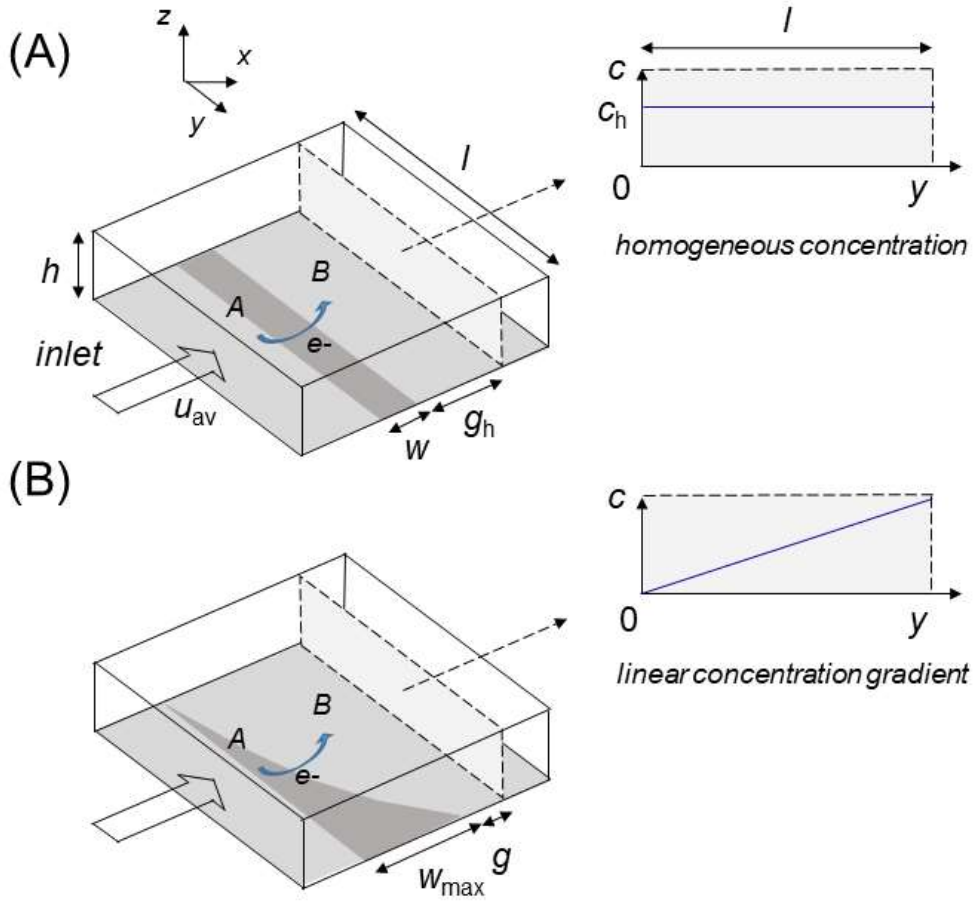

Figure 1. Schematic representation of working electrode operations within rectangular microchannels. **(**A) Case of a microband electrode leading to the generation of homogeneous concentration c_h at distance g_h. (B) Case of an electrode with optimized geometry leading to the generation of a linear concentration gradient perpendicular to the flow field at distance g.

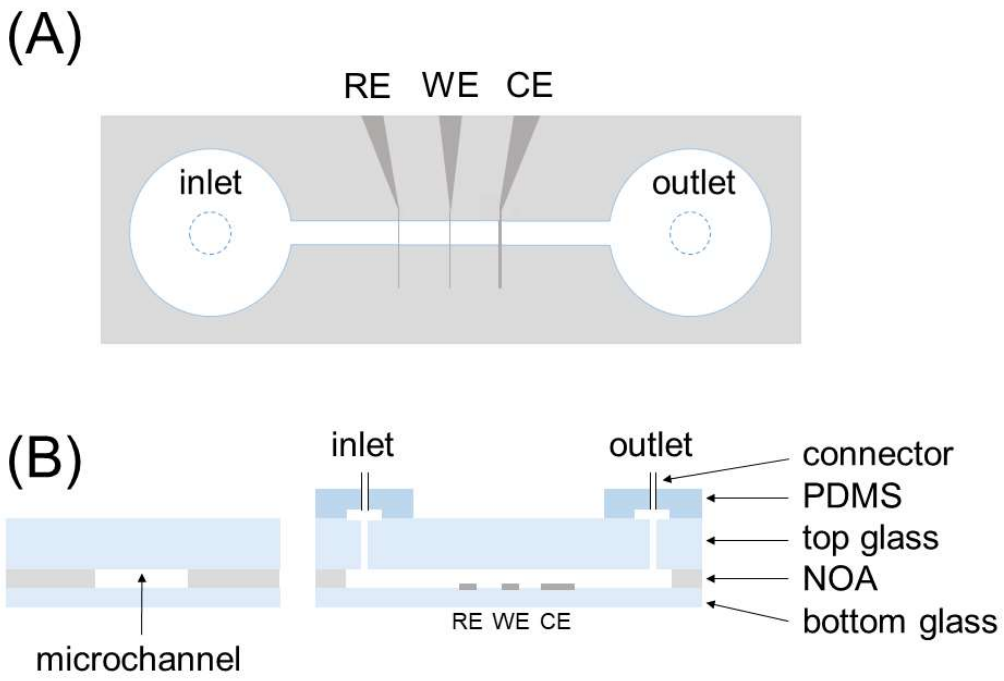

Figure 2. Schematic views of the NOA-glass hybrid microdevice. (A) Top view showing the microchannel, its reservoirs, and positioning of the three electrodes with their contact pads: reference electrode RE, working electrode WE and counter electrode CE. (B) Side views showing the multi layers with two glass sheets for top and bottom, and NOA as sidewalls of the microchannel. The schematic views are not at scale. Dimensions are indicated in experimental section.

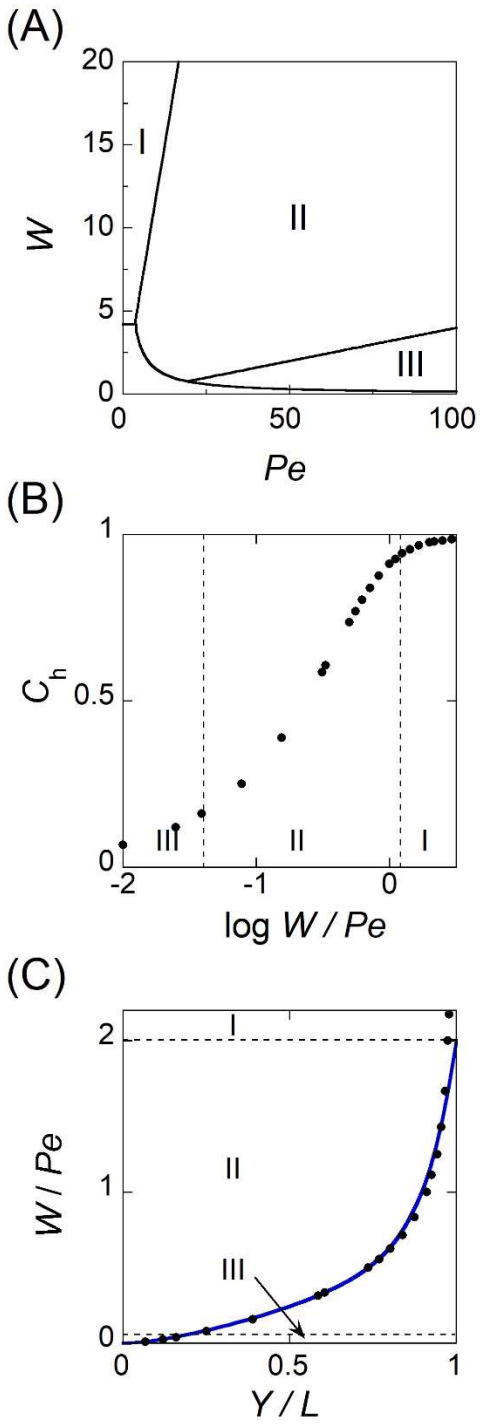

Figure 3. Operating regimes simulated at a microband electrode. (A) Zone diagram showing the regimes (I to III) according to the operating conditions (*W*,*Pe*). (B) Homogeneous concentration C_h of species generated downstream of the electrode as a function of *W*/*Pe*. (C) Predicted variation of the ratio *W*/*Pe* along the microchannel width *L* to generate downstream a linear concentration gradient. Data from (B) (dots) fitted by eq 2 (solid curve). In (B,C), the dashed lines delimit the operating regimes (I to III) on *W*/*Pe* axis. (*WPe*) > 15.

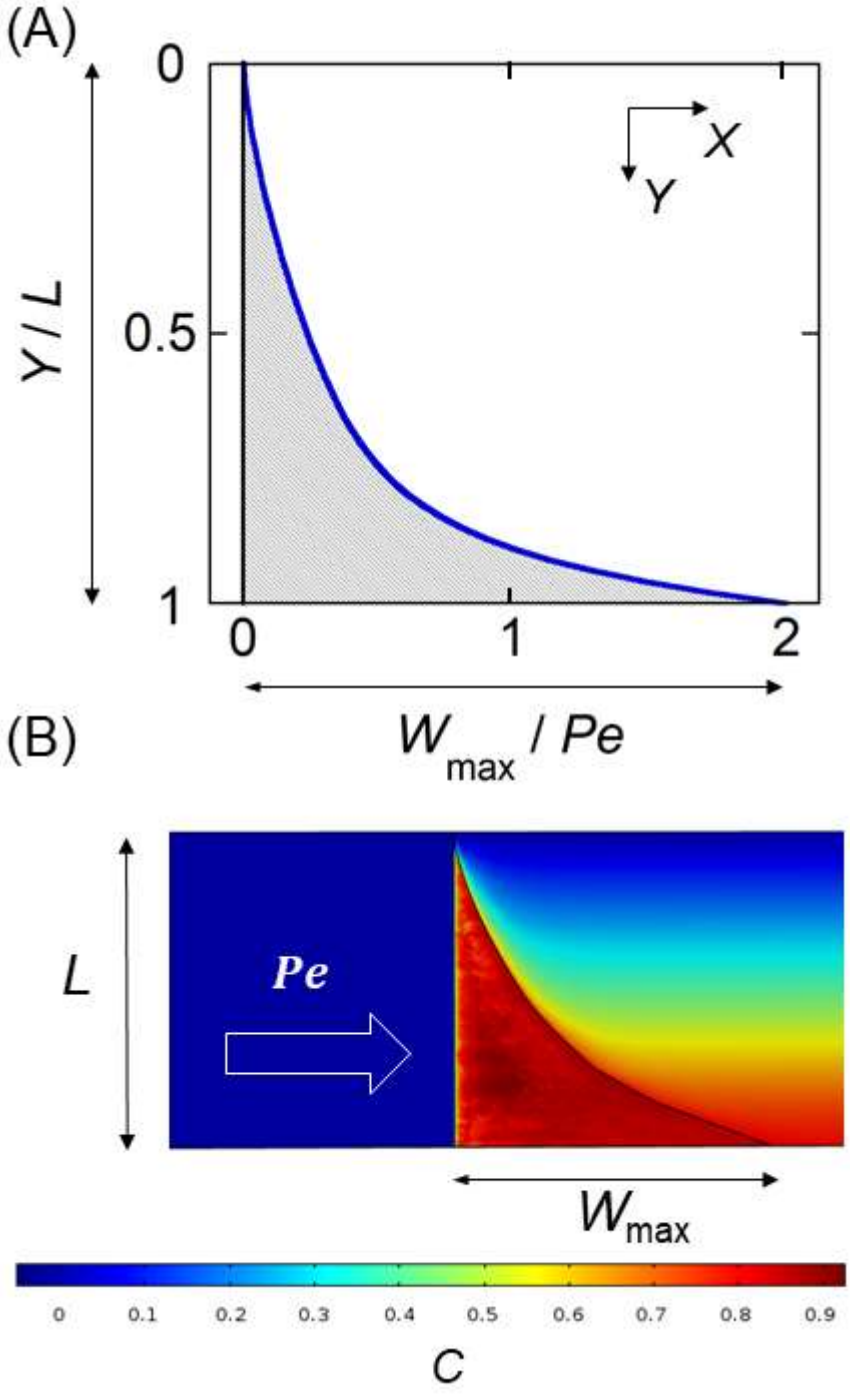

Figure 4. Optimized electrode geometry to generate downstream a linear concentration gradient. (A) Representation of the electrode shape on the microchannel floor. (B) Simulated concentration profiles of generated species. W_{max} = 80, L = 40 and Pe = 40. In (A,B), the Y-scale is expanded twice.

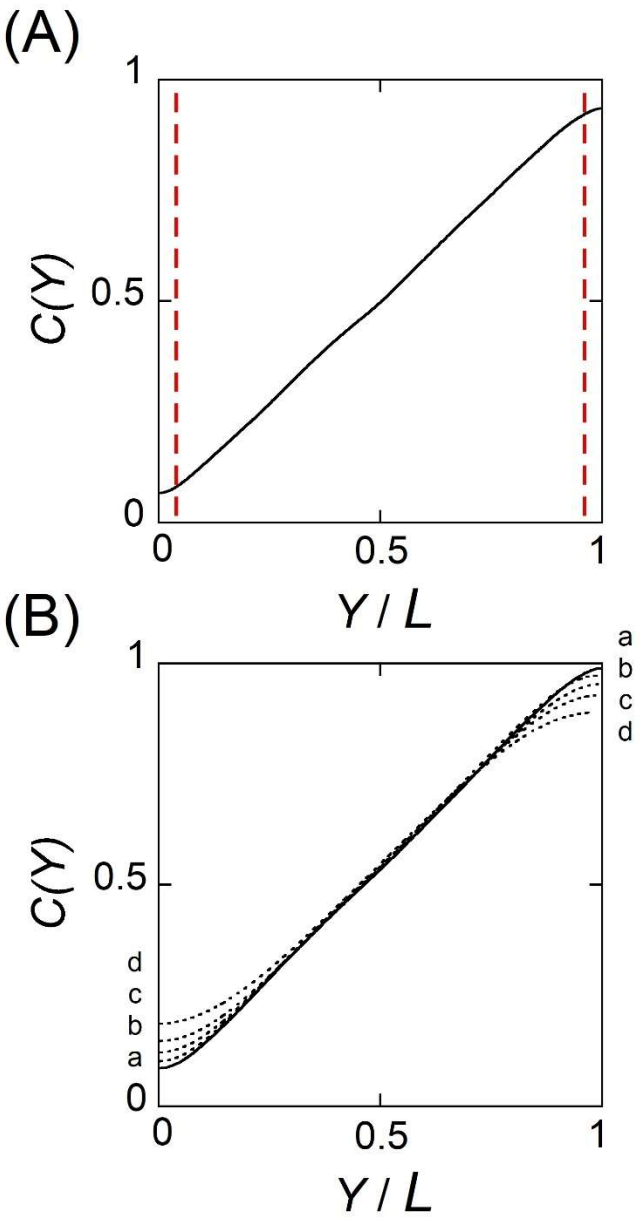

Figure 5. Simulated concentration gradients at several distances from the electrode. (A) Concentration profiles simulated at the distance G_h for several couples (W_{max},Pe): (20,10), (40,20), (60,30), (80,40), (100,50) and (200,100). $L = 40$. The dashed lines delineate zones due to sidewall effects. (B) Concentration profiles simulated at distances G_h (solid line), $10G_h$ (a), $25G_h$ (b), $50G_h$ (c) and $100G_h$ (d). $W_{max} = 80$, $L = 40$ and $Pe = 40$.

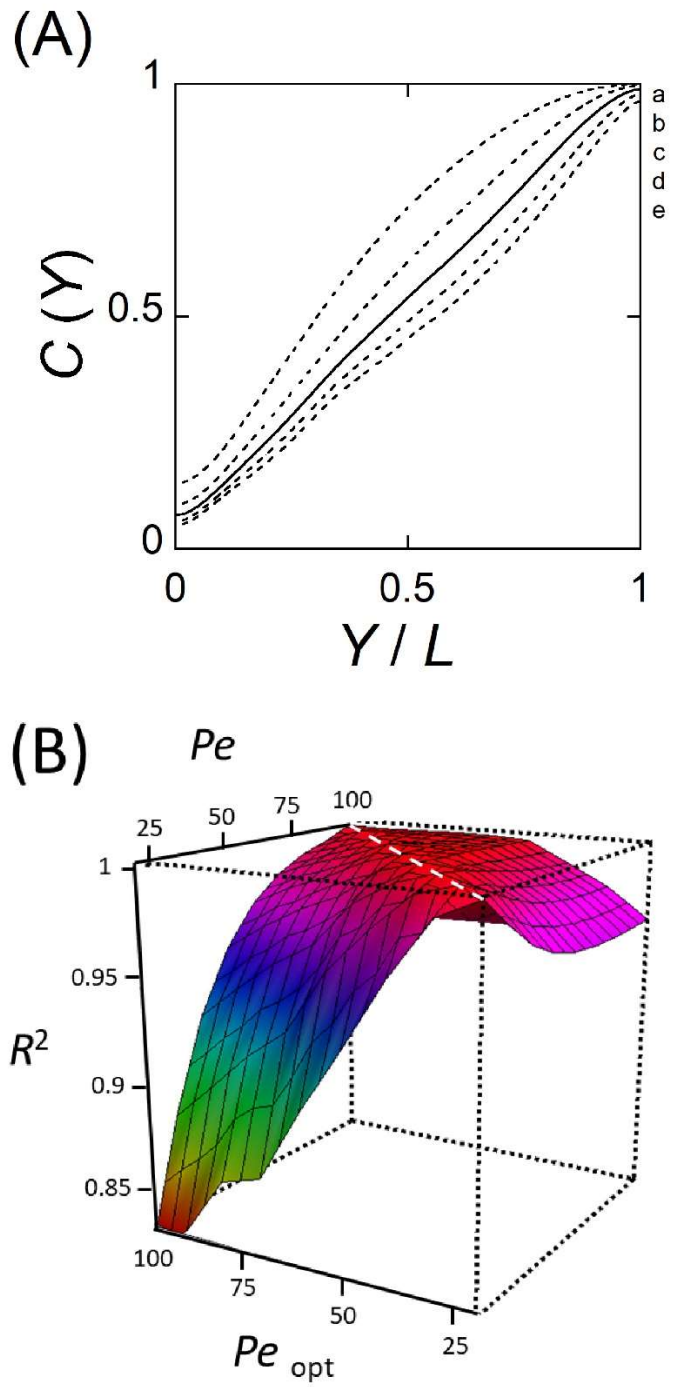

Figure 6. Influence of *Pe* on simulated concentration gradients at distance G_h = 0.4 Pe_{opt}. (A) Simulated concentration gradients at *Pe* = 20 (a), 30 (b), 40 (c), 50 (d) and 60 (e). W_{max} = 80, *L* = 40 and *Pe* = 40. (B) R^2 values from simulated concentration gradients as a function of *Pe* and Pe_{opt}. Values calculated for 0.04 < *Y*/*L* < 0.96, *L* = 40, 40 < W_{max} < 200 and 20 < *Pe* < 100. The white dashed line corresponds to the condition *Pe* = Pe_{opt} = W_{max} / 2.

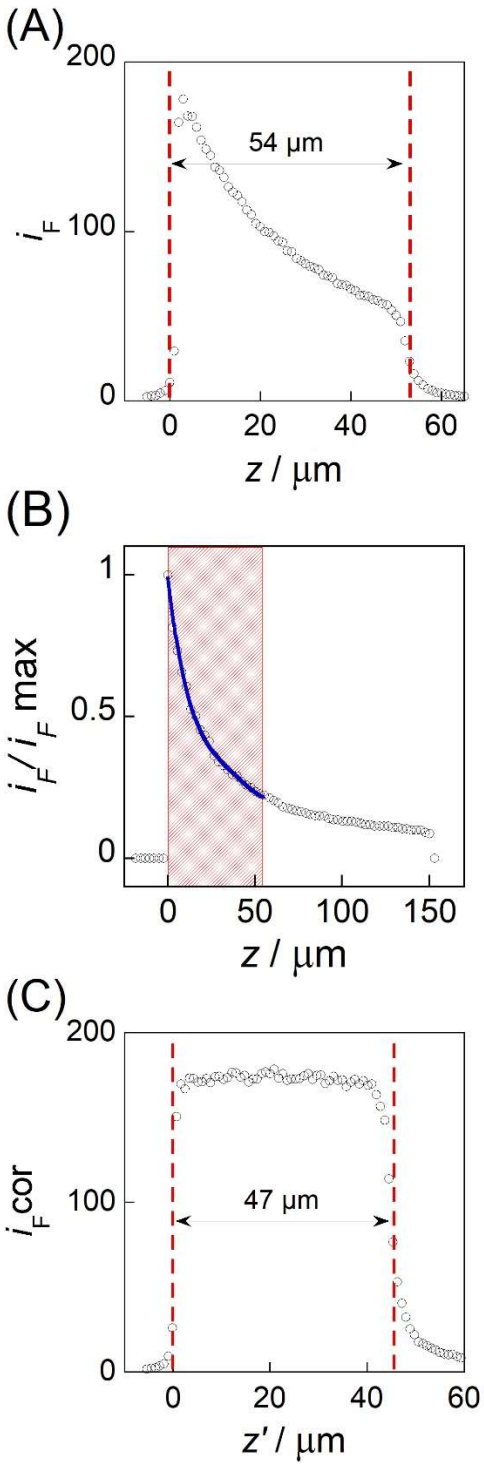

Figure 7. Fluorescence light intensity as a function of vertical distance. (A) Microdevice filled by a solution of 8 10^{-6} mol L^{-1} fluorescein, pH = 8. (B) Drop of 30 µL fluorescein 10^{-5} mol L^{-1} solution deposited on a glass slide, pH = 8; experimental data (symbols) and calibration curve (solid blue line). (C) Corrected fluorescence intensity profile deduced from data in (A). In (A) and (C) the channel height was 47 µm.

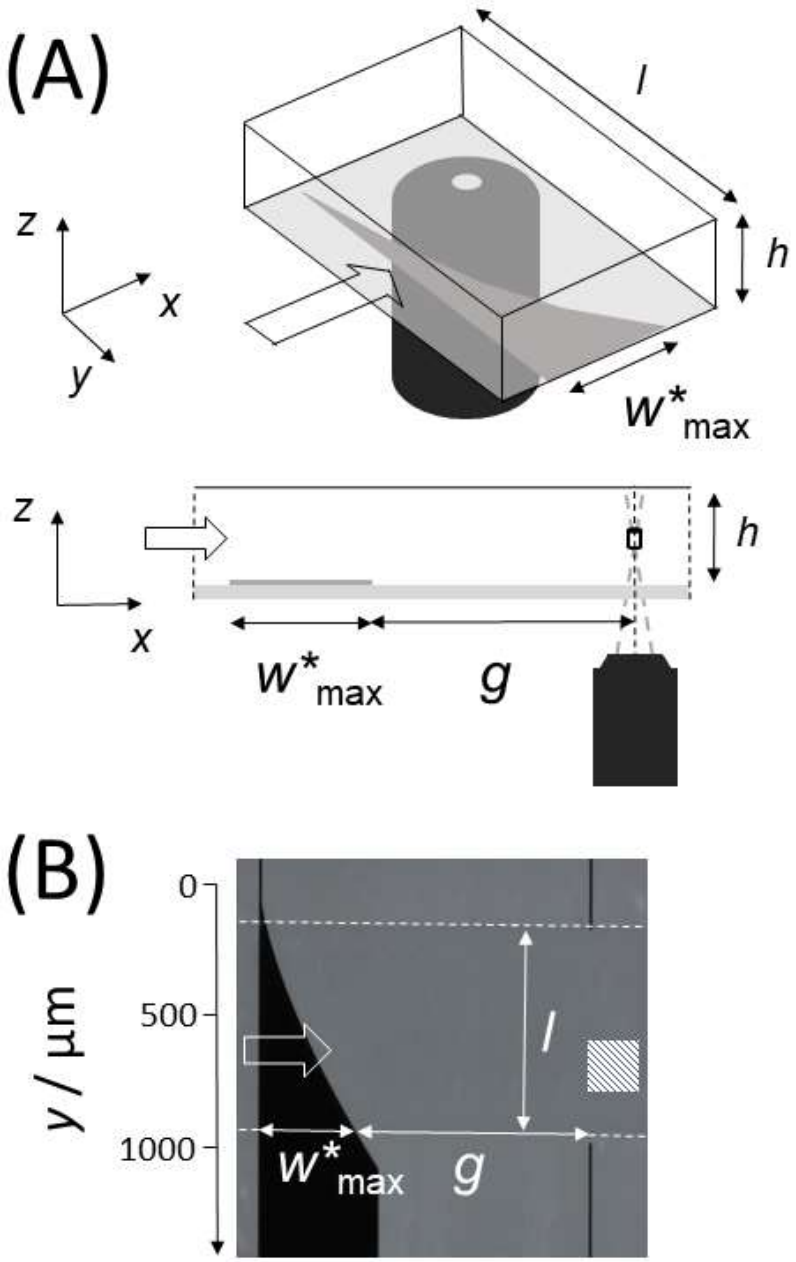

Figure 8. Experimental setup for generating and probing linear concentration gradients. (A) Schematic representation of fluorescence mapping by confocal microscopy. (B) Top-view photo of the electrode within the microchannel. Electrode designed for $Pe_{opt} = 40$ and $L = 40$. The black lines are optical markers. The superimposed dashed lines delimit the microchannel sidewalls whereas the superimposed hatched area locates the probed zone (212 µm x 212 µm). The reference electrode and counter electrode are located outside the optical field, respectively upstream (left side) and downstream (right side). Characteristics of microdevice: $l = 780$ µm, $h = 47$ µm, $w^*_{max} = 300$ µm, and $g = 880$ µm.

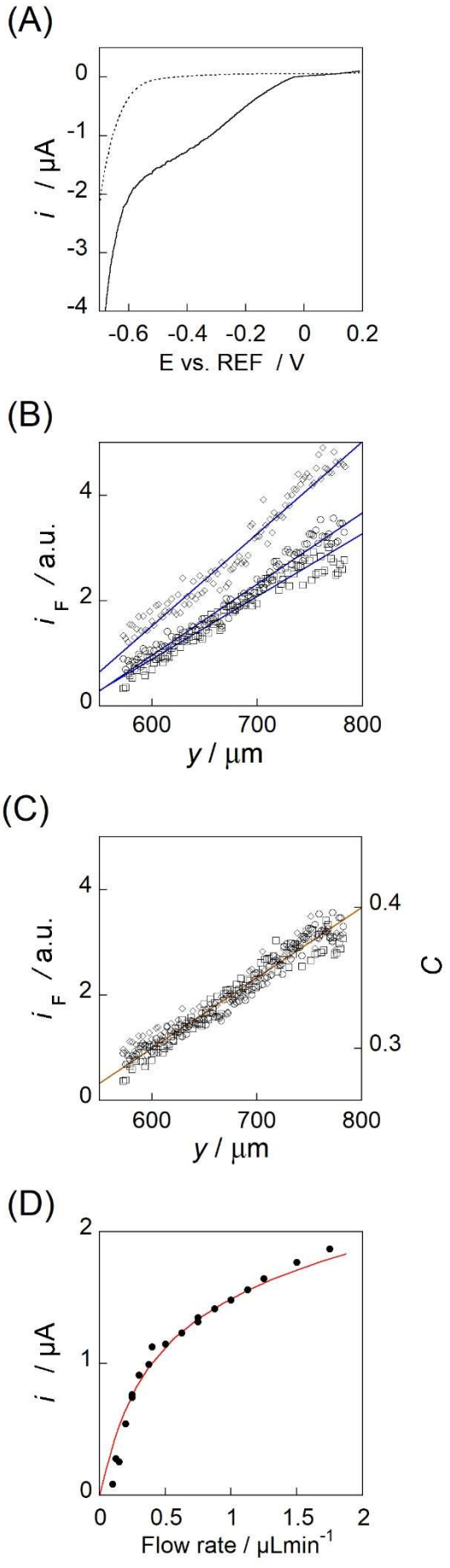
(A)
0
-1
-2
-3
-4
i / µA
-0.6
-0.4
-0.2
0
0.2
E vs. REF / V
(B)
4
2
0
i F / a.u.
600
700
800
y / µm
(C)
4
2
0
i F / a.u.
0.4
0.3
C
600
700
800
y / µm
(D)
2
1
0
i / µA
0
0.5
1
1.5
2
Flow rate / µLmin-1

Figure 9. Experimental data. (A) Steady-state voltammograms in 0.2 mol L^{-1} KCl (dashed line) with addition of benzoquinone $c_{BQ} = 10^{-3}$ mol L^{-1} (solid curve). **(**B) Fluorescence light intensities as a function of y for three vertical distances z within the microchannel; $z = 16.9$ µm ($z' = 14.7$ µm, diamantes), $z = 26.9$ µm ($z' = 23.5$ µm, circles) and $z = 36.9$ µm (z '= 32.2 µm, squares); linear regressions (blue lines). (C) Corrected fluorescence intensities from data in (A) and comparison with theoretical concentration profile (red line). In (A,B,C), flow rate 1.5 µL min^{-1}. (D) Current intensity of electrode as a function of flow rate with experimental (solid circles) and simulated data (red curve). $c_{BQ} = 10^{-3}$ mol L^{-1} / 0.2 mol L^{-1} KCl.

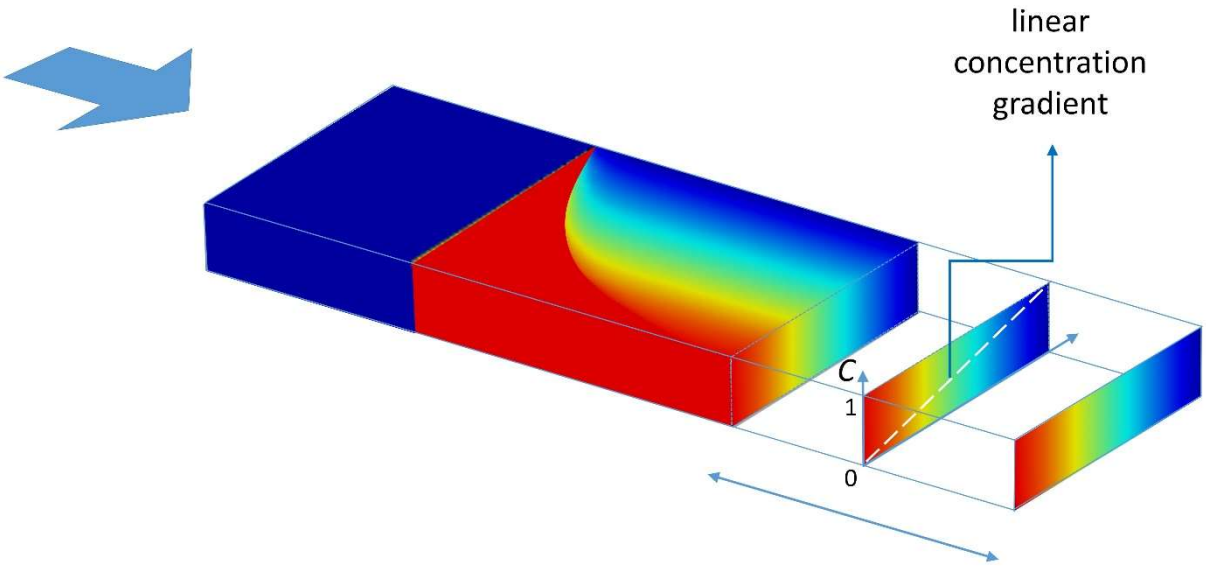

For TOC only.